Micromachined Heterostructured Lamb Mode Waveguides for Acoustoelectric Signal Processing

Hakhamanesh Mansoorzare, *Member, IEEE*, and Reza Abdolvand, *Senior Member, IEEE*

***Abstract*— This work explores micromachined heterostructured waveguides that leverage strong interactions between acoustic phonons and electrons to enable radio frequency (RF) signal amplification or attenuation. A thin-film piezoelectric-on-semiconductor stack is tailored to generate high electromechanical coupling Lamb waves that are impacted by high mobility electrons within a microacoustic waveguide. Lamb waves are generated by RF signal via interdigital electrodes on the piezoelectric layer; by applying a voltage to the semiconductor layer so that the electrons lead mechanical waves, the RF signal is amplified through the acoustoelectric (AE) effect. Conversely, the signals propagating faster or in the opposite direction of the electron flow undergo attenuation, rendering the waveguide nonreciprocal. Research on the AE effect dates to the mid-20th century and until now has been mostly focused on surface acoustic waves (SAWs). In this work, enabled by high-quality bonded thin films of lithium niobate (LN) and silicon (Si), it is shown that fundamental symmetric (*S*0) Lamb mode waveguides at 100 s of MHz can achieve more than 40 dB of AE gain and strong nonreciprocal transmission with less than 10 mW of bias power consumption. This could enable implementation of switches, delay lines, isolators, and circulators, which are critical for interference cancellation and full-duplex radio. The AE effect is observed to be stronger in some higher *S*0 harmonics, allowing for scaling to higher frequencies with optimized electrodes that have more relaxed critical dimensions. In addition, up to 5.5-dB sustained terminal gain measured in this work implies the potential for transistor-less amplifiers that could be implemented in concert with more traditional acoustic devices in a single-chip manner.**

***Index Terms*— Acoustoelectric (AE) effect, amplifier, delay line, heterostructure, Lamb wave, lithium niobate (LN), nonreciprocal, phonon–electron, piezoelectric, waveguide, wideband.**

I. Introduction

THE lower loss and significantly slower velocity of ultrasonic waves relative to electromagnetic signals have led to their widespread application in radio frequency (RF) signal processing with stringent performance and size specifications. For example, in today's connected world, microacoustic devices are becoming omnipresent by providing clock signals or frequency band selection [1]. However, the increased connectivity and data calls for additional signal processing capabilities that are not currently available in the microacoustic domain. Among said capabilities are signal isolation and interference cancellation that are crucial for wireless communication in a highly congested frequency spectrum. For example, full-duplex radio, which ideally doubles the spectral efficiency, requires large amounts of isolation and interference cancellation that are not currently practical. This must be performed across different domains such as antenna and digital backend, but generally, more than 50-dB RF/analog cancellation is needed [2], [3]. While nonreciprocal components, such as isolators and circulators, could partially fulfill this, they are mostly based on magnets, therefore, bulky, lossy, and incompatible with chip integration [4]. The remaining cancellation can be achieved by predicting the interference and timely subtracting it from the main receiving signal. It has been shown that the interference can be reconstructed from multiple weighted and delayed versions of the original signal [5]. This would require real-time delays that will be orders of magnitude smaller if realized in the microacoustic domain. These two examples would require nonreciprocity and tunable gain/loss, which once available in the microacoustic domain could allow for chip-scale isolation/cancellation.

It is well reported that electrons interact with acoustic waves and can lead to their amplification or attenuation [6]. Using piezoelectric substrates to launch surface acoustic waves (SAWs) and semiconductors to enable electron drift at the vicinity of the SAW and in parallel with it, it has been shown that SAW is amplified in the direction of electron flow and attenuated in the opposite direction. Through this phenomenon, also known as the acoustoelectric (AE) effect, amplifying and nonreciprocal SAW devices have been realized. The limitations of this approach, however, have resulted in far from ideal performance, such as high power consumption, low thermal stability, narrow bandwidth, and limited operation frequency [7]. These are further discussed in Section II. In this work, it is shown that a tailored thin-film piezoelectric-semiconductor platform could support strong interactions between high electromechanical coupling Lamb waves and high mobility electrons. Lamb waves, with respect to SAW, have higher phase velocity and stronger electric and stress field confinement. This results in higher frequency, lower

Manuscript received 18 April 2022; revised 15 July 2022; accepted 19 July 2022. Date of publication 8 August 2022; date of current version 4 November 2022. This work was supported by the National Science Foundation under Grant 1810143 and Grant 2122670. *(Corresponding author: Hakhamanesh Mansoorzare.)*

The authors are with the Department of Electrical and Computer Engineering, University of Central Florida, Orlando, FL 32816 USA (e-mail: hakha@knights.ucf.edu).

Color versions of one or more figures in this article are available at https://doi.org/10.1109/TMTT.2022.3194723.

Digital Object Identifier 10.1109/TMTT.2022.3194723

loss, and larger bandwidth. From waveguides micromachined in a thin-film lithium niobate (LN) on silicon (Si) stack, more than 40 dB of AE gain and nonreciprocal transmission is measured with a dc bias; in a typical device, with passband around ~615 MHz, the transmission ranges from +5.5 dB to −40 dB (background noise) as the bias is reduced from 125 to 0 V. Moreover, the continuous-wave terminal gain is sustained by a constant bias (~6.5 mW), due to the high power handling of the device as a result of Si underlayer. By providing a delayed signal within a passband that is tunable in amplitude and nonreciprocal in transmission, the presented waveguides could be used to form circulators or interference cancellation modules once used as an array. The organization of the rest is as follows. In Section II, a short background is presented on the AE effect. In Section III, the design and fabrication of the devices are described. The measurement results are presented in Section IV.

II. AE Effect

A. Concept

In a piezoelectric medium, the acoustic wave is coupled with an electric field as captured by the general constitutive equations of piezoelectricity

$$D = dT + \varepsilon^T E$$
$$S = d^t E + s^E T \tag{1}$$

where D is the electrical displacement, d is piezoelectric constant, T is stress, ε^T is the permittivity at constant stress, E is the electric field, S is the strain, s^E is compliance at a constant electric field, and the superscript t stands for matrix transposition. In a piezoelectric insulator, where there are no charge carriers, said electric field is not screened and not attenuated. Conversely, in a piezoelectric semiconductor, the acoustic wave induces an accompanying space charge wave that does not necessarily establish instantly and rather with a time constant. Such delay, which is a function of geometry, distributed resistance, and capacitance, causes the charge wave to lag the acoustic wave, thus leading to the attenuation of acoustic wave [8]. In the case of a propagating acoustic wave and majority electron carriers, electrons would bunch in potential minima and trail behind; increased electron density in regions with aligned electric field and acoustic wave vector causes attenuation due to potential to kinetic energy conversion from coupled electric field to electrons. To overcome this loss, said lag must be eliminated. This can be achieved by applying an electric field (E_D) along the acoustic wave vector so that the electrons drift with a velocity equal to the acoustic phase velocity. Since the drift velocity (v_D) is the product of the electron mobility (μ) and E_D, a larger μ would lower E_D needed for synchronization velocity, thus reducing the needed dc voltage. By further increasing E_D, v_D would exceed acoustic phase velocity (v_A); at this point, electrons start leading the acoustic wave, to which they lose momentum and cause traveling acoustic wave amplification. While described for a piezoelectric semiconductor, this phenomenon can be well extended to a piezoelectric insulator having a semiconductor medium nearby. In such case, an evanescent electric field in the semiconductor would interact with its charge carriers.

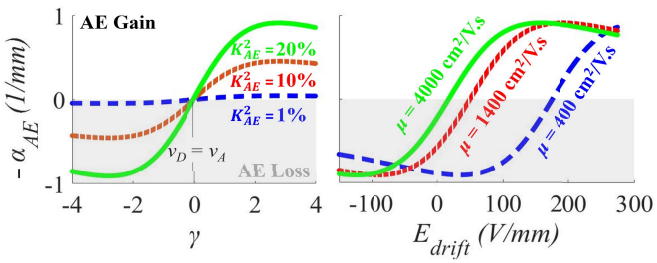

Fig. 1. AE gain coefficient versus relative velocities of electron drift and acoustic wave (γ) for different AE coupling values (left) and as a function of applied drift field for different electron mobilities (right).

In an intuitive manner, this phenomenon can be modeled with an *RC* system [9]. In this way, the AE attenuation coefficient (α_{AE}) can be expressed using few parameters, most importantly, the coupling between the electrons and acoustic wave (K^2_{AE}) and the *RC* time constant (τ). Both parameters depend on the system geometry; the former is bounded by the piezoelectric coupling and the latter depends on the effective permittivity and conductivity

$$\alpha_{\mathrm{AE}}/k_0 = K^2_{\mathrm{AE}}/2\big(\gamma\,\omega\tau/1 + (\gamma\,\omega\tau)^2\big). \tag{2}$$

In (2), k_0 is the wavenumber, ω is the angular frequency, and γ is a normalized difference between v_D and v_A (3); τ is proportional to the permittivity of the piezoelectric (ε_p) and semiconductor (ε_s) films and the inverse of the effective conductivity of semiconductor film (σ), as seen from (4)

$$\gamma = 1 - v_D/v_A \tag{3}$$
$$\tau = \big(\varepsilon_s + \varepsilon_p\big)/\sigma. \tag{4}$$

The AE attenuation or amplification—the sign of α_{AE}—is captured by the sign of γ: a negative γ, or $v_D > v_A$, yields a negative α_{AE}, which corresponds to AE gain. Since the parenthesis on the right-hand side in (2) takes a maximum of 0.5, the maximum possible value for the left side is $K^2_{\mathrm{AE}}/4$. This occurs once $\gamma\,\omega\tau$ equals unity, allowing for optimization of σ at the operating regime (ω, γ) for improving performance; this translates to optimizing the semiconductor doping (n). It is worth mentioning that the maximum gain and optimized n will be impacted by charge diffusion, trapping, and large-signal effects that are not considered in the presented model for simplicity. Nevertheless, to attain the highest gain at the lowest electric field or voltage, both K^2_{AE} and μ are desired to be maximized. The impact of said parameters on the AE gain coefficient ($-\alpha_{\mathrm{AE}}$) is shown in Fig. 1. Increasing K^2_{AE} scales the curve up in magnitude, while increasing μ shifts it toward smaller drift fields. Note that at $\gamma = 0$ or the synchronization velocity, α_{AE} becomes zero.

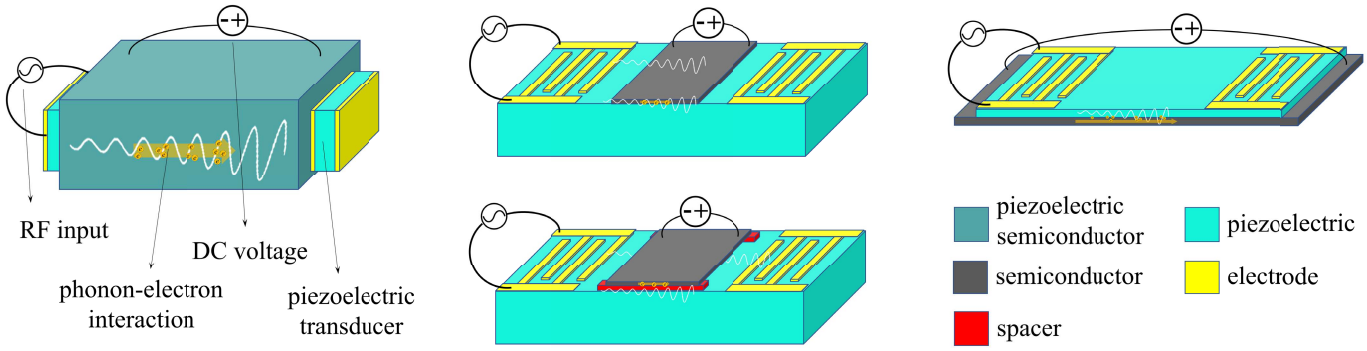

Fig. 2. Various AE amplifiers using (left) a piezoelectric-semiconductor slab for BAW amplification; (middle) layered SAW amplifiers with the semiconductor film directly deposited on or held with a small gap above the piezoelectric substrate; and (right) suspended heterostructure for Lamb wave amplification (this work).

B. Brief History

Research on the AE effect dates to the 1940s when it was observed that acoustic waves are attenuated by plasma. Later, in 1953, the term "AE" was coined once a dc current was detected in parallel with traveling longitudinal acoustic waves [6]. The possibility of amplification of the acoustic waves through the same mechanism was suggested in 1956 [10] and experimentally proven in 1961 [11]. To do so, a slab of cadmium sulfide, which is a piezoelectric semiconductor, was simultaneously injected with supersonic electrons and bulk acoustic waves (BAWs), leading to BAW amplification. Nevertheless, the low electron mobility in conventional piezoelectric semiconductors required impractically high voltages, in the kilovolt range. This problem triggered the idea of using SAW on a piezoelectric substrate and at the vicinity of a high-electron-mobility semiconductor [12]. In this way, the coupling between piezoelectrically generated evanescent electric field and electrons in the adjacent semiconductor results in signal amplification in a manner similar to traveling-wave tubes [13]. To efficiently excite SAW, a periodic pattern of electrodes that matches the SAW wavelength was used for the first time, marking the origin of interdigital transducers (IDTs) in 1965 [14]. This led to numerous demonstrations of AE SAW devices for amplification, sustained oscillation, and convolving. In such demonstrations, the semiconductor layer is either deposited on top [15] or held above the piezoelectric substrate [16] on the SAW propagation path. In the latter case, an extremely small gap is needed for maintaining sufficient AE coupling, which renders fabrication challenging, especially in terms of scalability. The monolithic version, on the other hand, calls for an ultrathin deposited semiconductor layer to still support the SAW. Despite all the efforts, it was soon recognized that with the available thin-film technology, such components cannot be practically implemented. The major issue was the transfer or growth of ultrathin semiconductors with low interface traps and low impact on the electron mobility and SAW. Therefore, those efforts resulted in very high power consumption, low efficiency, and poor noise performance.

By the end of the 20th century, due to its high mobility, 2-D electron gas (2DEG) was considered for improving the device performance [17] although poor piezoelectric properties of the material that readily form 2DEG resulted in weak interactions between SAW and 2DEG [18]–[20]. The advances in growth, transfer, and bonding of high-quality thin films in the past few years have boosted the performance of SAW AE devices, although ultrathin-film deposition with high electron mobility remains challenging. More recent works are mostly based on LN due to its large piezoelectric coupling and mature SAW backbone [21]–[24]. However, a major limitation of SAW is its scalability to higher frequencies before the losses and small feature sizes become problematic—often below 3 GHz. Suspended piezoelectric thin-film technology has enabled low-loss Lamb mode devices with higher phase velocities, therefore increasing the operation frequency [25]. More recently, Lamb modes in heterostructured suspended platforms have been investigated for the AE effect. These have been based on aluminum nitride on Si [26] and Ge [27] as well as LN on Si [28]–[30]. Suspended LN has shown excellent electromechanical properties, enabling large bandwidths and very low losses [31]; addition of a thin layer of Si underneath the LN has allowed for efficient AE interactions with superior power handling compared to SAW demonstrations [32]. Therefore, in this work, the LN on Si platform is further investigated for realizing high-performance AE devices. The presented structure is schematically compared with the previous demonstrations in Fig. 2.

III. LN on Si Waveguides

A. Design

The intensity of AE interactions is determined by the coupling between the piezoelectric evanescent electric field and the adjacent free electrons. As a result, having a high electromechanical coupling (K^2) and high spatial overlap between the evanescent field and free electrons is desired. Micromachined waveguides formed in LN thin films have shown promising performance in terms of loss and bandwidth by confining the electric and mechanical energy within their body. Since LN is highly anisotropic, its cut and orientation must be carefully selected to achieve the desired performance. Among the different cuts and orientations of LN, some of the highest values for K^2 have been reported for X-cut LN. These

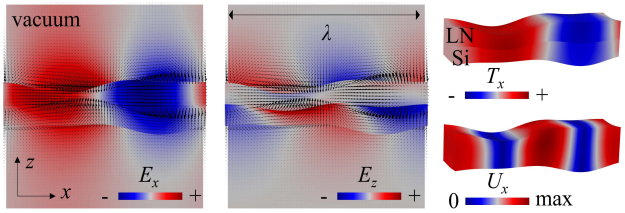

Fig. 3. Electric field along wave propagation (E_x) and thickness (E_z) of the LN/Si waveguide as well as the lateral stress (T_x) and displacement (U_x).

include close to 40% for SH0 mode oriented ~170° and 30% for $S0$ mode oriented ~30° off $+Y$-axis [33]. Since the latter has higher phase velocity, ~7000 versus ~4400 m/s, which allows for higher frequency, it has been targeted in this study. Fig. 3 shows the lateral and vertical electric field as well as the stress and displacement of $S0$ mode in LN/Si (1/1 μm) stack within a wavelength (λ). The evanescent electric field effectively extends by $1/k_0$, which for instance is only 1.6 μm at $\lambda = 10$ μm. While such thickness for the Si underneath LN could provide a complete overlap between electrons and the electric field, further reducing the Si thickness relative to that of LN would boost K^2 of the stack. Therefore, it is desired to have the thinnest Si but without introducing surface nonidealities such as scattering and degradation of electron mobility. The effect of X-cut LN orientation and Si thickness on K^2 is shown in Fig. 4. The K^2 dispersion is calculated using (5) in which the $S0$ phase velocity in two cases of electrically open (v_O) and short (v_S) is simulated using a COMSOL model. Said electrical boundary conditions are applied to the top surface of LN film and the results are plotted for the $Y30°$ orientation of a 1/1μm LN/Si stack in Fig. 4 at few wavelengths of this study. For comparison, these simulations are performed for the stack without the Si layer as well

$$K^2 = \left(v_O^2 - v_S^2\right)/v_O^2. \tag{5}$$

While the addition of the Si underlayer reduces K^2, a relatively large value is still expected for the cases having thin Si. To excite and detect the Lamb waves, IDTs are deposited on top of the LN layer at the two ends of the waveguide. The IDT periodicity defines the passband of the waveguide. Lamb waves at such frequencies travel within the waveguide, interacting with electrons in Si. As a result, the gain/loss is selectively applied to the allowed modes and specifically the ones with the highest K^2. This is achieved by biasing the Si layer through specific contacts positioned outside of the suspended waveguide; depending on the relative velocities of Lamb waves and drifting electrons, the energy would transfer from one to the other. Having dc contacts outside of the wave propagation path is another advantage of this platform compared to SAW counterparts where dc contacts positioned within the SAW path cause additional perturbations.

With limiting the loss to mechanical damping and neglecting the AE interactions, a 2-D COMSOL model is used to study the effect of some of the device parameters on its transmission frequency response. In Fig. 5, the effect of the Si thickness,

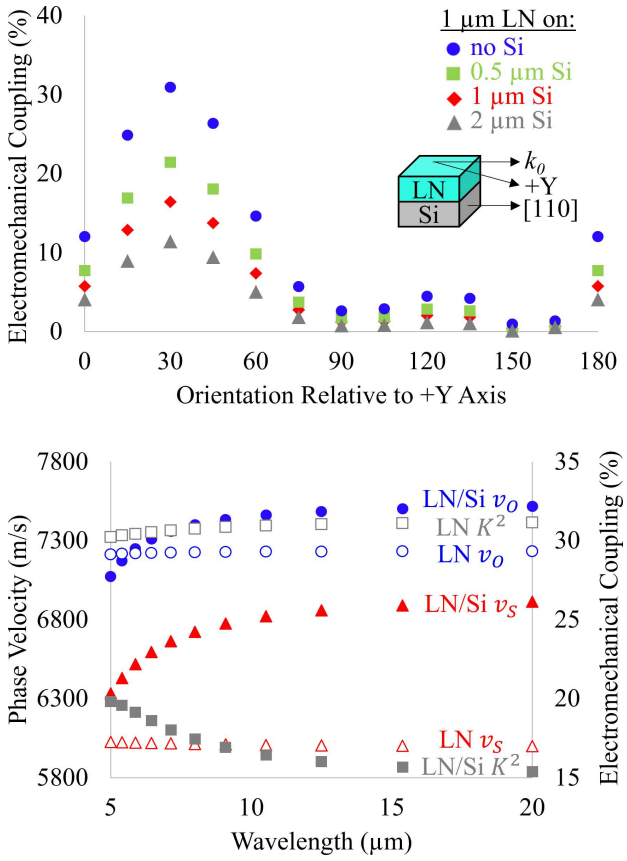

Fig. 4. Electromechanical coupling dispersion for different orientations of LN relative to Si and for different Si thicknesses (top). Phase velocity and electromechanical coupling as a function of wavelength for 1/1 μm LN/Si when LN is $Y30°$ oriented as well as LN by itself (bottom).

the number of IDT finger pairs, IDT thickness, and IDT finger pitch (FP) is shown. In these simulations, the IDT has basic bidirectional design and is made of gold (Au), the Si thickness is 1 μm, the number of IDT pairs is five in each port, IDT thickness is 100 nm, and IDT FP is 5 μm, once they are not the parameter under study. Perfectly matched layer (PML) is used at both ends of the waveguide to eliminate reflections from terminated waveguide boundaries. It is notable that a wider bandwidth is realized with reducing IDT pairs but at the cost of a higher transmission loss (see Fig. 5). In addition, the mechanical impact of the IDT thickness and material warrants careful optimization to attain the desired performance. Changing the IDT pitch from 10 to 3 μm covers a frequency range of ~700 MHz on the same stack and for scaling to higher frequencies a thinner stack is needed. The width of the waveguide is defined by etching the stack and should be significantly larger than λ to limit the diffraction losses.

The IDT FP can be constant or varied across the width or length of the waveguide as a mean of increasing its bandwidth. By including a range of IDT periodicities rather that a single value, a wider range of wavelengths would be transduced, however, this comes at the cost of insertion loss (IL). With respect to varying the IDT FP across the

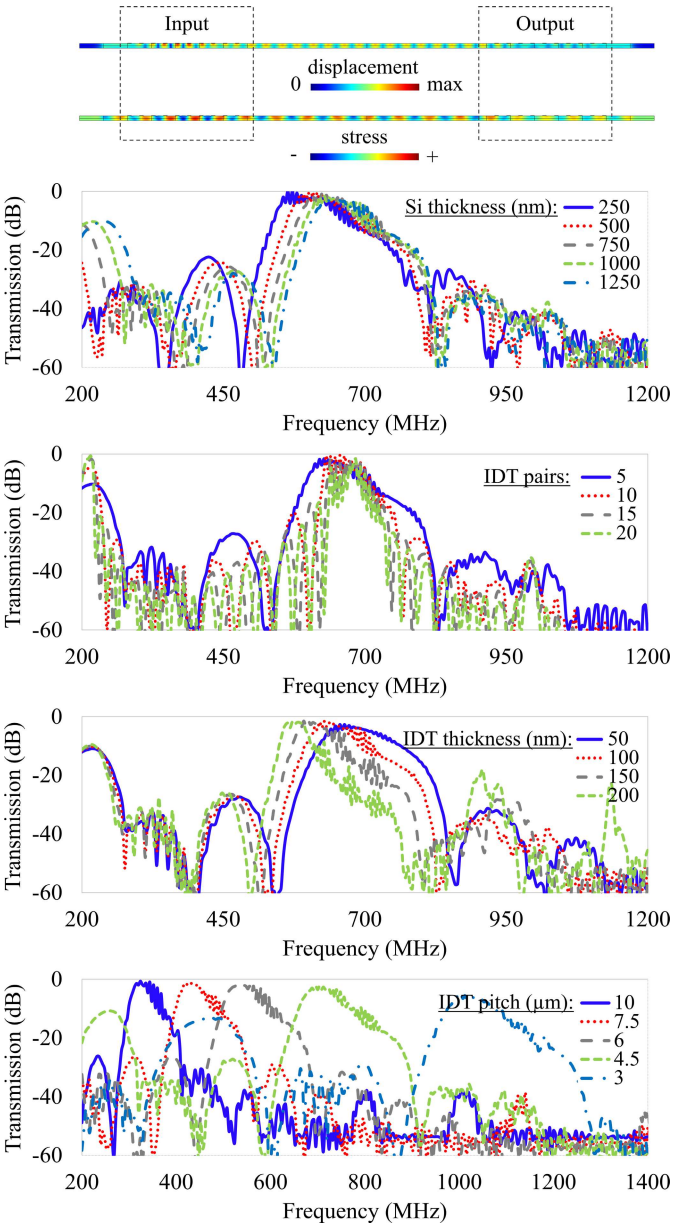

Fig. 5. Transmission of waveguides simulated by COMSOL in 2-D. The control device is made of 1/1 μm LN/Si with a gap of 400 μm and IDT FP of 5 μm made of five pairs. First, the effect of the Si thickness is shown. Second, the effect of the number of IDT pairs is shown. Third, the effect of the thickness of IDT is shown. Fourth, the effect of the IDT FP is shown.

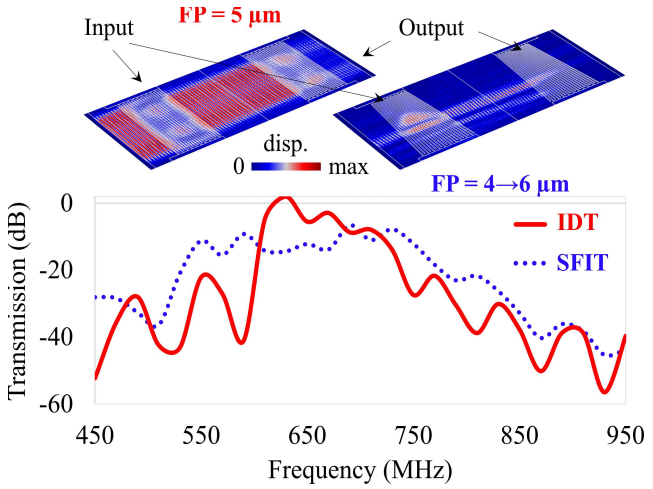

Fig. 6. COMSOL simulated displacement of two waveguides at 610 MHz one with regular IDT and the other one with SFIT, showing significant diffraction in the latter (top). SFIT allows for a wider bandwidth but more lossy transmission (bottom).

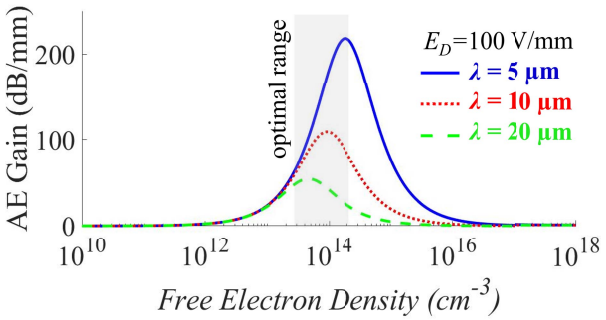

Fig. 7. Effect of free electron density in Si on the AE gain at different wavelengths and a fixed applied drift field.

device width, or aperture, slanted-finger IDTs (SFITs) have been used for wideband SAW devices [34]. This concept can be simply viewed as multiple fixed-FP IDTs with very narrow aperture in parallel. The sub-IDT FP can be linearly or nonlinearly changed from the lowest to the highest value for designing a flat passband. The application of SFIT has also been explored in Lamb mode waveguides, resulting in an improved 6-dB below peak fractional bandwidth ($FBW_{6\,dB}$) of ~8% [35]. However, the reported IL is high (>26 dB), especially due to the substantial diffraction losses associated with this type of transducers. This is due to the narrow aperture of each fixed-FP sub-IDT, which cannot be much enlarged as the increased ohmic losses become significant, especially at higher frequencies. The 3-D COMSOL simulated transmission response of two similar waveguides one having fixed-FP IDT of 5 μm and the other one having SFIT with a linearly swept FP of 4 to 6 μm is shown in Fig. 6. The region between the two-port IDTs is roughly 200 μm × 200 μm and the wave diffraction seen from the displacement profile at 610 MHz is evident for SFIT. Leveraging AE amplification, in this case, could enable wideband Lamb mode waveguides with low loss.

The Si doping, as mentioned earlier, would impact the device performance and must be optimized based on the operation regime, i.e., frequency and drift field. Fig. 7 shows the effect of free electron concentration in Si on the AE gain (2) at $\lambda = 5$, 10, and 20 μm, and $E_D = 100$ V/mm. Ignoring charge trapping and diffusion, n-type doping in the order of 10^{14} cm^{-3} is expected to maximize the AE gain and is chosen in this work. The trapping will manifest itself in shifting the optimal doping range, reducing the effective electron mobility, and most importantly limiting the attainable noise performance. The latter can be improved by understanding the time constant

associated with the traps and operating at a frequency where $1/\omega$ is far away from such time constant.

B. Fabrication

The waveguides are fabricated in a five-mask process with the starting substrate provided by NGK Insulators Ltd. The substrate is made of 4" X-cut LN wafer that is bonded to a 4" silicon on insulator (SOI) with 3-μm (100) device layer using surface activation bonding. The bonded LN wafer is subsequently polished down to 1 μm, while the SOI layer is etched down to 1 μm in a later step. The LN film is oriented in a way that the wave propagation axis is aligned to both the $\sim$30° off $+y$-axis direction of LN and the [110] Si plane for maximizing the electromechanical coupling of the $S0$ mode. The Si layer is n-type doped with a 5–10-Ω.cm resistivity. The IDT is made of e-beam evaporated Cr/Au (25/75 nm) patterned by liftoff. Next, using argon (Ar) plasma, contacts to the Si layer are made by etching through the LN layer. This is done in an inductively coupled plasma/reactive ion etching (ICP/RIE) tool with a $\sim$3-μm plasma enhanced chemical vapor deposition (PECVD) Si dioxide (SiO_2) mask. The Si openings and the IDT probe pads are overlaid with e-beam evaporated Cr/Au (25/75 nm) to improve electrical contact. The lateral boundary of the device and current isolation trenches is defined by dry etching the LN/Si in Ar plasma followed by deep reactive ion etching (DRIE). The patterning is performed using a $\sim$3-μm PECVD SiO_2 mask that is patterned in CHF_3 plasma with a $\sim$4.5-μm photoresist mask. RCA1 cleaning is intermittently performed during the LN etching to remove the etching byproducts. The wafers are subsequently flipped, and the backside ($\sim$375 μm) is patterned with $\sim$12-μm photoresist and etched in DRIE. This is followed by releasing the devices in buffered oxide etch (BOE). The SOI layer is finally thinned to 1 μm in a SF_6/C_4F_8 plasma from the backside. In Fig. 8, the bonded wafer is shown and the fabrication steps are summarized. The scanning electron micrograph (SEM) of a typical waveguide and close-up of the IDT, the LN/Si stack, and the SFIT are shown in Fig. 9.

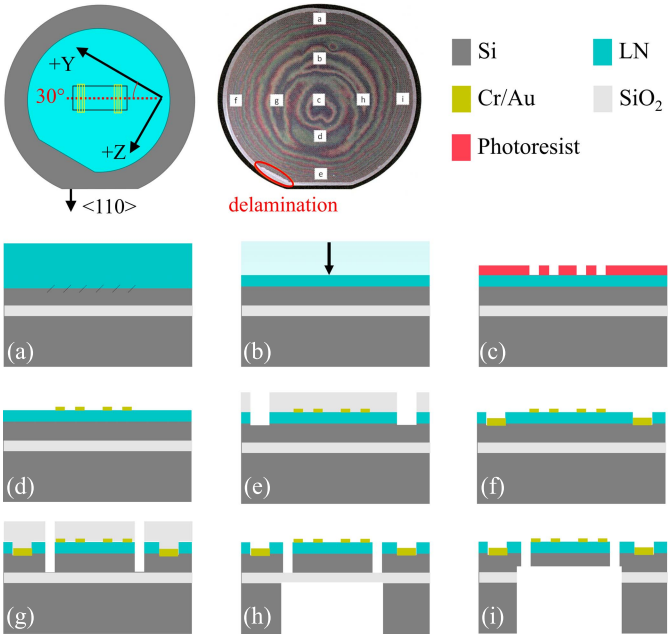

Fig. 8. Fabrication process. (a) Bonding LN to SOI. (b) Polishing LN down to 1 μm. (c) and (d) Patterning top electrodes via liftoff. (e) Etching LN to open Si contacts. (f) Overlaying Si openings and RF pads with Au. (g) Etching the lateral device boundaries. (h) Etching the backside of the SOI wafer. (i) Releasing the device and thinning Si from backside.

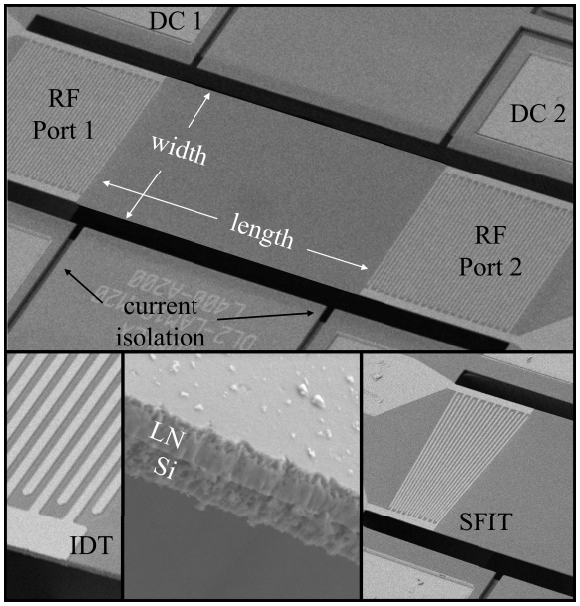

Fig. 9. SEM of typical fabricated waveguides and features.

IV. Measurement Results

The fabricated devices are characterized at room temperature and in atmospheric pressure by a network analyzer (Rhode and Schwarz ZNB 8) using ground signal ground (GSG) microprobes (Cascade Microtech Inc.). Prior to measurements, a short-open-load-thru calibration is performed to set the reference planes at the microprobe tips. All the measurements are performed at an input RF signal level of -20 dBm, unless otherwise mentioned.

A. Passive Waveguides

The waveguides in the passive state (i.e., without any dc bias applied to Si for electron drift) show a large IL and reciprocal transmission from one port to another. The main source of such high loss is the presence of the Si layer. This is experimentally validated by completely etching Si from the backside in SF_6/C_4F_8 plasma so that the waveguide is only made of LN. Typical transmission response of a 700-μm-long waveguide before and after the Si removal is shown in Fig. 10 in solid red and dashed blue, respectively. The device IL within its passband ($\sim$615 MHz) is improved from $\sim$51 to 7.5 dB, showing $\sim$43.5-dB added loss from Si. While different factors, such as reduced coupling, LN–Si interface loss, and the AE loss, contribute to such added loss, the latter is the main contributing factor. This was confirmed by observing a continuous increase in the device IL as the original

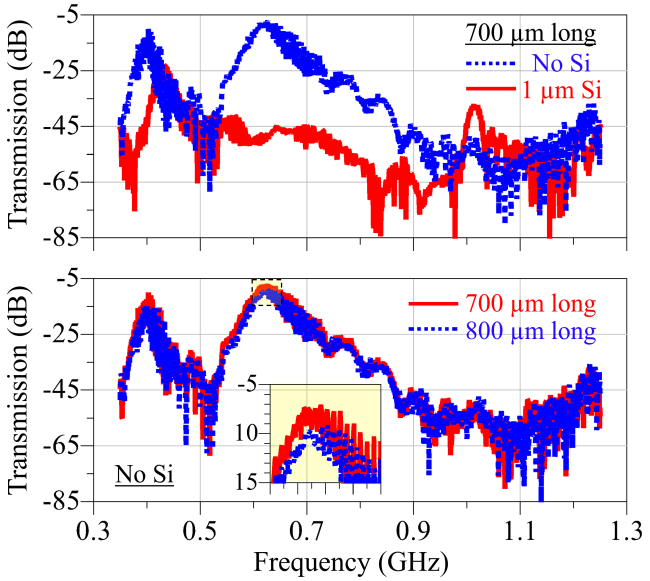

Fig. 10. Measured transmission of a passive waveguide (700 μm long) with 1-μm Si under 1-μm LN and with completely etched Si (top). The effect of propagation loss in LN on transmission seen for two waveguides, 700 and 800 μm long, after removing Si (bottom).

SOI layer was thinned from 3 to 1 μm. The transmission peak observed at ~400 MHz corresponds to the SH0 mode and its lower AE coupling can be inferred from the smaller change of IL after Si removal. In addition, from the devices with removed Si, the $S0$ wave propagation loss in LN is estimated; by comparing the IL of identical devices with the lowest loss but different lengths, this is determined to be close to 12 dB/mm. Since this is much larger than the best reported value of 0.8–2.3 dB/mm [36], it implies further opportunity for optimization of the film quality and fabrication. The effect of the propagation loss in LN on the transmission of 700- and 800-μm-long devices is shown in Fig. 10, in solid red and dashed blue, respectively. Since the measurements are performed in a 50-Ω system and the IDT impedance of devices has not been specifically designed for 50 Ω, for the gain measurements in Sections IV-B and IV-C, the mismatch losses (3–5 dB) are eliminated by impedance matching using Advanced Design System (ADS) software.

B. Biased Waveguides

Using a pair of dc probes, from the Si openings at the two ends of the waveguides, the biasing voltage is applied to cause electron drift. As the voltage is increased, $S0$ mode transmission in the direction of the electron drift gradually improves. The same behavior is observed for the reverse isolation since waves in the opposite direction undergo AE attenuation, reducing backward transmission. Therefore, the nonreciprocal contrast is intensified by increasing the bias and its direction depends on bias polarity. This is clearly seen in waveguides with OFF-state (passive) transmission well above the background noise, which is due to various sources of leakage between the two ports. The magnitude of transmission

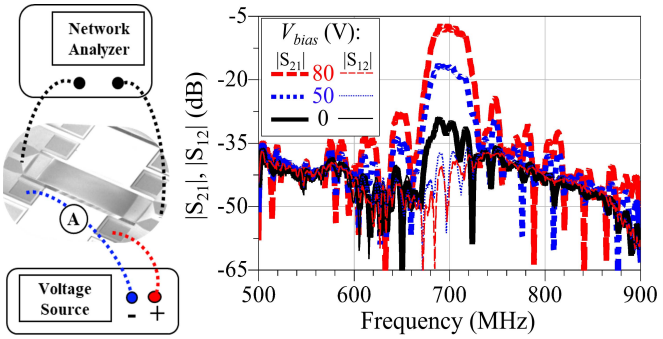

Fig. 11. Measurement setup (left) and the effect of bias voltage on reducing the transmission loss and increasing nonreciprocal contrast ($|S_{21}| - |S_{12}|$) measured for a 400-μm-long waveguide (right).

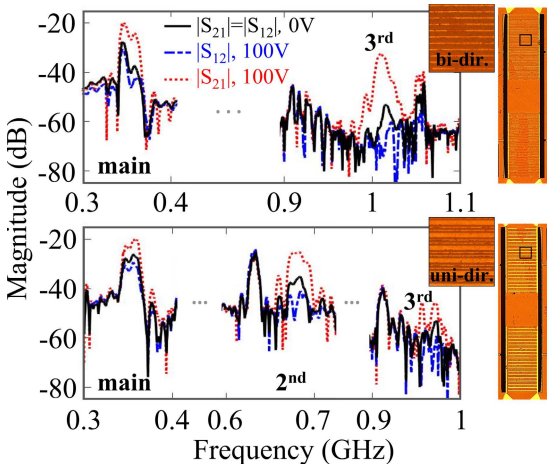

Fig. 12. Frequency response of $\lambda = 20$ μm (~360 MHz) waveguides having bidirectional (top) and single-phase unidirectional (bottom) IDT for nonreciprocal transmission at higher harmonics.

in forward ($|S_{21}|$) and backward ($|S_{12}|$) for a 400-μm-long waveguide having a 5-μm FP is shown in Fig. 11 for three bias levels. At zero bias, the transmission is reciprocal as evident from the overlapping solid thick and thin black curves. Increasing the bias moves $|S_{21}|$ upward (thick lines) and $|S_{12}|$ downward (thin lines), as plotted at 50 V in dotted blue and 80 V in dashed red. The latter bias yields a total AE gain of 22 dB and a nonreciprocal contrast of >30 dB. Once bias is increased beyond this point, S_{12} remains at the background level while S_{21} starts degrading due to large-signal and thermal effects.

The nonreciprocal behavior is observed for higher $S0$ harmonics as well. This is shown for two waveguides (see Fig. 12) designed with their fundamental mode at $\lambda = 20$ μm (~360 MHz) while having different IDT configurations [37] that allow for a notable second or third harmonic nonreciprocal transmission. At 100 V, the waveguide with single-phase unidirectional transducer shows 17-dB nonreciprocal contrast at second harmonic (~680 MHz), while the one with simple bidirectional IDT—having <40% electrode coverage—shows 38-dB nonreciprocal contrast at third harmonic (~1 GHz). As expected from the theory, a stronger nonreciprocity can be obtained at higher frequencies.

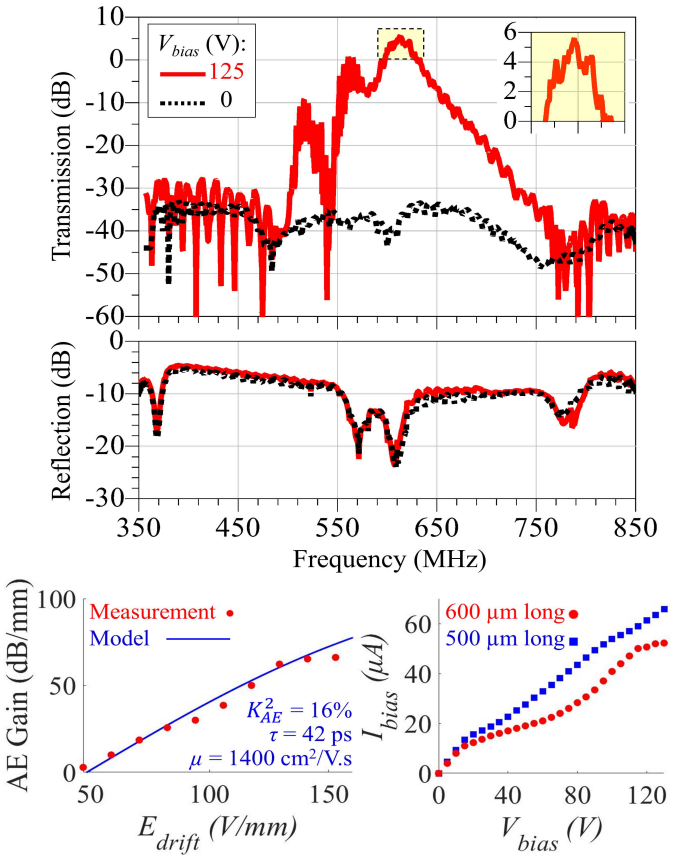

Fig. 13. Measured transmission and reflection of a 600-μm-long waveguide at 0- and 125-V bias (top). Measured AE gain as a function of electric field fit with the *RC* model (bottom left). Bias current–voltage characteristic of two waveguides having different lengths (bottom right).

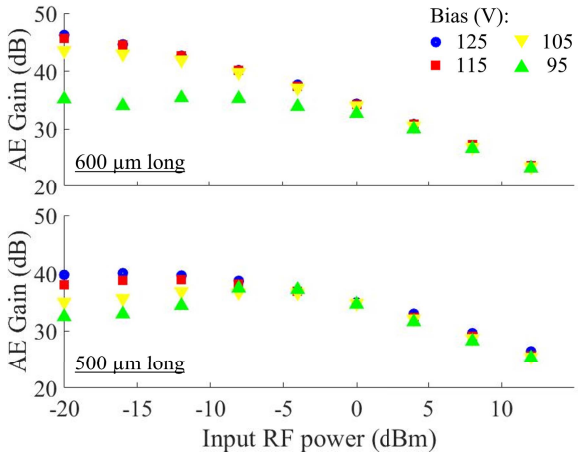

Fig. 14. Measured AE gain compression characteristic of 500- and 600-μm-long devices at different bias voltages.

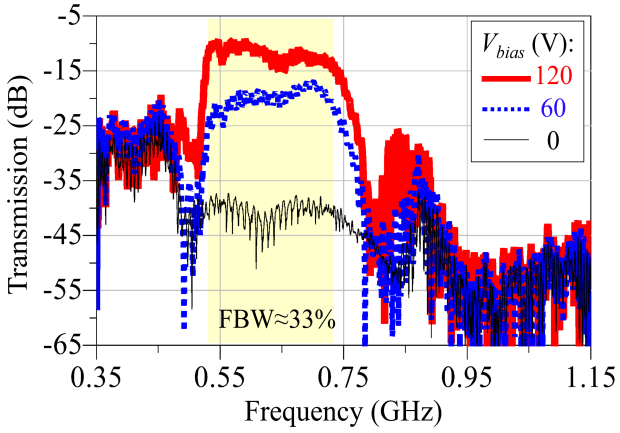

Fig. 15. Measured transmission of a wideband 600-μm-long waveguide having SFIT at both ports. The FP is linearly increased from 4 to 6 μm and a bandwidth of 215 MHz is covered with 6 dB of ripple.

To further increase the AE gain without reaching the large-signal and thermal limitations, a longer waveguide is required. While this would increase the required bias voltage for a given drift field, increasing the phonon–electron interaction length can not only compensate for the entire signal losses, whether from IDTs or propagation loss, but also amplify the original signal to yield terminal gain. This is shown for a 600-μm-long device in Fig. 13 where at 125-V bias, the transmission peak is +5.5 dB at ~615 MHz. The measured terminal gain is realized in a sustained manner with a continuous RF signal and bias and no need for pulsed operation. The dissipated bias power, in this case, is estimated to be less than 6.5 mW, by measuring ~50 μA of dc current passing the waveguide. The measured AE gain versus the applied electric field is shown in Fig. 13 and fit with the *RC* model (2). The bias voltage–current characteristic of waveguides (plotted for 500- and 600-μm-long devices in Fig. 13) shows a not entirely ohmic behavior and kinks likely due to electron scattering and AE current of amplified noise.

AE gain compression is observed by increasing the input RF power level. The bias and the device geometry also affect the gain compression characteristics. This is shown in Fig. 14 by comparing the total AE gain–the change of $|S_{21}|$ before and after bias—as a function of the input RF signal for 500- and 600-μm-long devices and at several bias levels. While smaller gains are measured from the shorter device for low input powers, gain compression starts at a higher input power in comparison with the longer waveguide.

C. Wideband Waveguides

AE gain and nonreciprocity within wider bandwidths are demonstrated in devices with SFIT [30]. The transmission of a device having linearly increasing FP from 4 to 6 μm is shown in Fig. 15. The device has a 600-μm mean distance between the two ports SFIT. The thin black curve is transmission at 0 V, which as expected lies at the background noise level. The dotted blue curve is transmission at 60 V and the red solid curve is at 120 V. At the latter bias, corresponding to 4.5-mW dc power dissipation, the peak transmission is measured to be −9.7 dB and the 6-dB below peak bandwidth is 215 MHz. This translates to a very large $\text{FBW}_{6\,\text{dB}}$ of ~33%. The transmission dips in the passband are believed to be due to the destructive interference of sub-IDTs and could be relieved by optimizing the SFIT design. As reported in [38], by using a stepped SFIT

TABLE I
SURVEY OF RECENT SAW AE PLATFORMS AND THIS WORK

Ref.	Platform	Freq. (MHz)	AE Gain (dB/mm)	Non-Reciprocity (dB)	Power (mW)	Continuous Bias
[22]	Si-LN	470	-	10	-	✓
[23]	Graphene-LN	170	9	16	137	✓
[24]	InGaAs-LN	276	80.6	46	15	✕
This work	**Lamb Mode LN-on-Si**	**~700**	**>40**	**>40**	**<10**	✓

design, the sub-IDT phases can be adjusted to reduce passband ripples.

V. CONCLUSION

It was demonstrated that micromachined Lamb mode waveguides made of piezoelectric on semiconductor could provide unprecedented functionalities such as nonreciprocal transmission and signal amplification by leveraging strong electron–phonon interactions known as the AE effect. The heterostructured design allows for independent choice of the piezoelectric and semiconductor to achieve the desired performance. This includes high electromechanical coupling, high electron mobility, and high power handling that are attained here by choosing LN and Si, as said layers. Through this platform, frequency disperse filters, delay lines, switches, amplifiers, isolators, and circulators could be realized all on a single chip, therefore significantly reducing packaging size, costs, and complexities. In Table I. some performance metrics of the presented Lamb mode platform are compared against the state of the art, which all rely on SAWs. Finally, noise performance is another important factor in the application of this platform. Internal noise figures as low as 6.5 dB have been preliminarily measured, being highly affected by the biasing conditions and contact resistances, which should be further investigated in future works.

REFERENCES

[1] R. Weigel *et al.*, "Microwave acoustic materials, devices, and applications," *IEEE Trans. Microw. Theory Techn.*, vol. 50, no. 3, pp. 738–749, Mar. 2002.

[2] S. Hong *et al.*, "Applications of self-interference cancellation in 5G and beyond," *IEEE Commun. Mag.*, vol. 52, no. 2, pp. 114–121, Feb. 2014.

[3] A. Sabharwal, P. Schniter, D. Guo, D. W. Bliss, S. Rangarajan, and R. Wichman, "In-band full-duplex wireless: Challenges and opportunities," *IEEE J. Sel. Areas Commun.*, vol. 32, no. 9, pp. 1637–1652, Sep. 2014.

[4] J. D. Adam, L. E. Davis, G. F. Dionne, E. F. Schloemann, and S. N. Stitzer, "Ferrite devices and materials," *IEEE Trans. Microw. Theory Techn.*, vol. 50, no. 3, pp. 721–737, Mar. 2002.

[5] D. Bharadia, E. McMilin, and S. Katti, "Full duplex radios," in *Proc. ACM SIGCOMM*, Aug. 2013, pp. 375–386.

[6] R. H. Parmenter, "The acousto-electric effect," *Phys. Rev.*, vol. 89, no. 5, p. 990, Mar. 1953.

[7] Y. V. Gulyaev and F. S. Hickernell, "Acoustoelectronics: History, present state, and new ideas for a new era," *Acoust. Phys.*, vol. 51, no. 1, pp. 81–88, Feb. 2005.

[8] M. Pomerantz, "Ultrasonic loss and gain mechanisms in semiconductors," *Proc. IEEE*, vol. 53, no. 10, pp. 1438–1451, Oct. 1965.

[9] R. Adler, "Simple theory of acoustic amplification," *IEEE Trans. Sonics Ultrason.*, vol. 18, no. 3, pp. 115–118, Jul. 1971.

[10] G. Weinreich, "Acoustodynamic effects in semiconductors," *Phys. Rev.*, vol. 104, no. 2, p. 321, Oct. 1956.

[11] A. R. Hutson, J. H. McFee, and D. L. White, "Ultrasonic amplification in CdS," *Phys. Rev. Lett.*, vol. 7, no. 6, p. 237, Sep. 1961.

[12] Y. V. Gulyaev and V. I. Pustovoit, "Amplification of surface waves in semiconductors," *Sov. Phys. JETP*, vol. 20, no. 6, p. 1508, Jun. 1965.

[13] R. Kompfner, "Travelling-wave tubes," *Rep. Prog. Phys.*, vol. 15, no. 1, p. 275, Jan. 1952.

[14] R. M. White and F. W. Voltmer, "Direct piezoelectric coupling to surface elastic waves," *Appl. Phys. Lett.*, vol. 7, no. 12, pp. 314–316, Dec. 1965.

[15] L. A. Coldren and G. S. Kino, "Monolithic acoustic surface-wave amplifier," *Appl. Phys. Lett.*, vol. 18, no. 8, pp. 317–319, Apr. 1971.

[16] K. M. Lakin, J. H. Collins, and P. J. Hagon, "100 MHz surface acoustoelectric amplifier exhibiting stable terminal gain with DC drift field," *Proc. IEEE*, vol. 57, no. 4, pp. 740–742, Apr. 1969.

[17] A. Wixforth, J. P. Kotthaus, and G. Weimann, "Surface acoustic waves on GaAs/Al_xGa_{1-x}As heterostructures," *Phys. Rev. B, Condens. Matter*, vol. 40, no. 11, p. 7874, Oct. 1989.

[18] L. Shao and K. P. Pipe, "Amplification and directional emission of surface acoustic waves by a two-dimensional electron gas," *Appl. Phys. Lett.*, vol. 106, no. 2, Jan. 2015, Art. no. 023106.

[19] H. Zhu and M. Rais-Zadeh, "Non-reciprocal acoustic transmission in a GaN delay line using the acoustoelectric effect," *IEEE Electron Device Lett.*, vol. 38, no. 6, pp. 802–805, Jun. 2017.

[20] S. Ghosh, T. Hancock, M. Storey, L. Parameswaran, M. Geis, R. Ralston, and D. Weinstein, "Nonreciprocal acoustoelectric interaction of surface waves and fluorine plasma-treated AlGan/GaN 2DEG," in *Proc. 19th Int. Conf. Solid-State Sens., Actuators Microsyst. (TRANSDUCERS)*, Jun. 2017, pp. 1939–1942.

[21] U. K. Bhaskar, S. A. Bhave, and D. Weinstein, "Silicon acoustoelectronics with thin film lithium niobate," *J. Phys. D, Appl. Phys.*, vol. 52, no. 5, Nov. 2018, Art. no. 05LT01.

[22] S. Ghosh, "FDSOI on lithium niobate using Al_2O_3 wafer-bonding for acoustoelectric RF microdevices," in *Proc. 20th Int. Conf. Solid-State Sens., Actuators Microsyst. Eurosensors XXXIII (TRANSDUCERS EUROSENSORS XXXIII)*, Jun. 2019, pp. 535–538.

[23] D. C. Malocha, C. Carmichael, and A. Weeks, "Acoustoelectric amplifier with 1.2-dB insertion gain monolithic graphene construction and continuous wave operation," *IEEE Trans. Ultrason., Ferroelectr., Freq. Control*, vol. 67, no. 9, pp. 1960–1963, Sep. 2020.

[24] L. Hackett *et al.*, "Towards single-chip radiofrequency signal processing via acoustoelectric electron–phonon interactions," *Nature Commun.*, vol. 12, no. 1, p. 2769, May 2021.

[25] S. Gong and G. Piazza, "Design and analysis of lithium-niobate-based high electromechanical coupling RF-MEMS resonators for wideband filtering," *IEEE Trans. Microw. Theory Techn.*, vol. 61, no. 1, pp. 403–414, Dec. 2013.

[26] H. Mansoorzare and R. Abdolvand, "Acoustoelectric amplification in lateral-extensional composite piezo-silicon resonant cavities," in *Proc. Joint Conf. IEEE Int. Freq. Control Symp. Eur. Freq. Time Forum (EFTF/IFC)*, Apr. 2019, pp. 1–3.

[27] F. Hakim, M. Ramezani, S. Rassay, and R. Tabrizian, "A non-reciprocal Lamb-wave delay line exploiting acoustoelectric effect in single crystal germanium," in *Proc. IEEE 33rd Int. Conf. Micro Electro Mech. Syst. (MEMS)*, Jan. 2020, pp. 1246–1249.

[28] H. Mansoorzare and R. Abdolvand, "Acoustoelectric non-reciprocity in lithium Niobate-on-Silicon delay lines," *IEEE Electron Device Lett.*, vol. 41, no. 9, pp. 1444–1447, Sep. 2020.

[29] H. Mansoorzare and R. Abdolvand, "A thin-film piezo-silicon acoustoelectric isolator with more than 30 dB non-reciprocal transmission," in *Proc. IEEE 34th Int. Conf. Micro Electro Mech. Syst. (MEMS)*, Jan. 2021, pp. 470–473.

[30] H. Mansoorzare and R. Abdolvand, "Ultra-wideband non-reciprocal micro-acoustic delay lines with slanted-finger interdigital transducers," in *Proc. IEEE 35th Int. Conf. Micro Electro Mech. Syst. Conf. (MEMS)*, Jan. 2022, pp. 1014–1017.

[31] R. Lu and S. Gong, "RF acoustic microsystems based on suspended lithium niobate thin films: Advances and outlook," *J. Micromech. Microeng.*, vol. 31, no. 11, Sep. 2021, Art. no. 114001.

[32] H. Mansoorzare, "Acoustoelectric amplification in piezoelectric-silicon micromachined Lamb wave devices," Ph.D. dissertation, Dept. Elect. Comput. Eng., Univ. Central Florida, Orlando, FL, USA, 2021.

[33] I. E. Kuznetsova, B. D. Zaitsev, S. G. Joshi, and I. A. Borodina, "Investigation of acoustic waves in thin plates of lithium niobate and lithium tantalate," *IEEE Trans. Ultrason., Ferroelectr., Freq. Control*, vol. 48, no. 1, pp. 322–328, Jan. 2001.

[34] A. P. Van den Heuvel, "Use of rotated electrodes for amplitude weighting in interdigital surface-wave transducers," *Appl. Phys. Lett.*, vol. 21, no. 6, pp. 280–282, Sep. 1972.
[35] N. Kuo, J. S. Fernandez, and G. Piazza, "1 GHz bulk acoustic wave slanted finger interdigital transducers in aluminum nitride for wideband applications," in *Proc. IEEE Int. Freq. Control Symp. (IFCS)*, May 2012, pp. 1–4.
[36] R. Lu, Y. Yang, and S. Gong, "Acoustic loss in thin-film lithium niobate: An experimental study," *J. Microelectromech. Syst.*, vol. 30, no. 4, pp. 632–641, Aug. 2021.
[37] H. Engan, "Excitation of elastic surface waves by spatial harmonics of interdigital transducers," *IEEE Trans. Electron Devices*, vol. 16, no. 12, pp. 1014–1017, Dec. 1969.
[38] G. Martin and B. Steiner, "SAW filters including one-focus slanted finger interdigital transducers," *IEEE Trans. Ultrason., Ferroelectr., Freq. Control*, vol. 50, no. 1, pp. 94–98, Jan. 2003.

Hakhamanesh Mansoorzare (Member, IEEE) received the B.S. degree from the Sharif University of Technology, Tehran, Iran, in 2016, and the M.S. and Ph.D. degrees from the University of Central Florida, Orlando, FL, USA, in 2020 and 2021, respectively, all in electrical engineering.

He is currently a Post-Doctoral Researcher with the University of Central Florida. His research interests lie in the area of microelectromechanical systems (MEMS) with a special focus on the design, fabrication, and characterization of piezoelectric devices for radio frequency signal processing and sensor applications.

Dr. Mansoorzare has won the Best Student Paper Award at the 2019 Joint Conference of the IEEE International Frequency Control Symposium and European Frequency and Time Forum. He was also the Finalist of the Outstanding Oral Paper Award at the 2021 IEEE International Conference on Micro Electro Mechanical Systems and the Finalist of the Best Poster Award at the Hilton Head Workshop 2022.

Reza Abdolvand (Senior Member, IEEE) received the Ph.D. degree from the School of Electrical and Computer Engineering, Georgia Institute of Technology, Atlanta, GA, USA, in 2008.

He was an Assistant Professor with the School of Electrical and Computer Engineering, Oklahoma State University, Stillwater, OK, USA. In 2014, he joined the University of Central Florida, Orlando, FL, USA, where he is currently a Professor and the Chair of the Department of Electrical and Computer Engineering. He has authored/coauthored two book chapters and more than 100 articles in his areas of research. He is also the inventor on 12 issued U.S. patents on concepts ranging from acoustic micro-devices to micro-fabrication technologies. His area of research interest lies in the general field of microelectromechanical systems (MEMS) with a special interest in piezoelectric microsystems. He is credited worldwide to have significantly contributed to the development of a class of microdevices that he has coined as thin-film piezoelectric-on-substrate (TPoS) resonators.